Article

Structure and Properties of NbMoCrTiAl High-Entropy Alloy Coatings Formed by Plasma-Assisted Vacuum Arc Deposition

Yurii F. Ivanov [1], Yuriy Kh. Akhmadeev [1], Nikita A. Prokopenko [1,*], Olga V. Krysina [1], Nikolai N. Koval [1], Elizaveta A. Petrikova [1], Oleg S. Tolkachev [1], Vladimir V. Shugurov [1], Vladimir V. Uglov [1,2] and Alexander N. Shmakov [1,3]

1   Institute of High Current Electronics SB RAS, 2/3 Akademichesky Ave., 634055 Tomsk, Russia; yufi55@mail.ru (Y.F.I.); ahmadeev@opee.hcei.tsc.ru (Y.K.A.); krysina@opee.hcei.tsc.ru (O.V.K.); koval@opee.hcei.tsc.ru (N.N.K.); petrikova@opee.hcei.tsc.ru (E.A.P.); ole.ts@mail.ru (O.S.T.); shugurov@opee.hcei.tsc.ru (V.V.S.); uglov@bsu.by (V.V.U.); highres@mail.ru (A.N.S.)
2   Department of Solid State Physics, Belarusian State University, 4 Nezavisimosti Ave., 220030 Minsk, Belarus
3   Budker Institute of Nuclear Physics SB RAS, 11 Akademika Lavrentieva Ave., 630090 Novosibirsk, Russia
*   Correspondence: prokopenko@opee.hcei.tsc.ru

Abstract: The paper analyzes the structure and properties of metal, cermet, and ceramic NbMoCrTiAl high-entropy alloy (HEA) coatings formed on solid substrates by plasma-assisted vacuum arc deposition (from multicomponent gas-metal plasma through Nb, Mo, Cr, and TiAl cathode evaporation in argon and/or a mixture of argon and nitrogen). The analysis shows that all coatings represent a nanocrystalline (3–5 nm) multilayer film. The metal coating has a bcc lattice ($a = 0.3146$ nm). The ceramic coating has an fcc lattice (an uncertain lattice parameter due to highly smeared diffraction peaks). The coating hardness increases in the order of metal, cermet, and then ceramic, reaching 43 GPa at Young's modulus equal to 326 GPa. When heated in air, the metal and cermet coatings start to oxidize at 630–640 °C, and the ceramic coating at 770–780 °C.

Keywords: plasma-assisted vacuum arc deposition; high-entropy alloy; metal, ceramic, and cermet coatings; synchrotron radiation; structure; properties

1. Introduction

High-entropy alloys (HEAs) and their carbides, nitrides, oxides, etc. [1–4] feature a unique combination of properties unattainable in most modern materials: high corrosion resistance [5,6], good mechanical characteristics at high [7] and low temperatures [8,9], high wear resistance [10,11], high strength and plasticity [12,13], high hardness (HEAs) and superhardness (ceramic HEAs) [14–19], etc. It can thus be expected that such alloys will find a wide range of applications in the industry in the near future [20–26].

For example, HEAs which are made as light as Al alloys but harder than certain types of metal glass [27] can find application in transport and energy technologies, where high-strength, light alloys are in great demand [28]. HEAs containing refractory Nb, Mo, and Ta are capable of preserving their high hardness even above 1200 °C, which makes them superior to conventional superalloys like Inconel 718 and Haynes 230 [7], and can be employed in gas turbines, jet nozzles, and nuclear reactors [29]. Low-density refractory HEAs can also be used in aerospace technologies for which light materials resistant to high temperature are needed [30]. The outstanding cryogenic properties of HEAs make them an excellent material for manufacturing rocket jackets, pipelines for liquid oxygen or nitrogen transport and storage [31]. As has been shown [21], HEAs can replace Ni-based refractory alloys and become next-generation refractory materials.

Among the promising HEA deposition technologies are plasma or thermal spraying in which HEAs in the form of rods and powders are melted and deposed on the surface of parts [32]. HEAs can be used for electromagnetic noise suppression, especially in

electronics [33], and their nitrides as well as HEAs as such for radiation-resistant coating deposition on fuel element shells [34], which extends the application of this type of material in high technologies.

Among the HEA nitride coatings with rather high functional properties obtained to date are (AlCrTaTiZr)N [15], (TiAlCrSiV)N [16], (AlCrMoSiTi)N [17], (AlMoNbSiTaTiVZr)N [18], (AlCrNbSiTiV)N [19], (TiVCrZrY)N [35], (TiVCrZrHf)N [36], (TiHfZrVNb)N [37], and (AlCrTiZrNbY)N [38].

The (AlCrTaTiZr)N and (TiVCrZrY)N coatings [15] were formed by reactive magnetron sputtering without substrate heating and substrate bias. They comprised a single fcc solid solution phase, and their microhardness measured 32 and 17.5 GPa, respectively. The coatings (AlCrTaTiZr)N [39], (AlCrNbSiTiV)N [19], and (AlMoNbSiTaTiVZr)N_x [18] were also deposited by reactive magnetron sputtering but with a substrate bias of −100 V and substrate heating to 373–773 K. They comprised only one fcc solid solution phase, and their microhardness measured 35 GPa, 41 GPa, and 37 GPa, respectively.

The conclusion is that nitride coatings based HEAs, like those based on transition metals, have a single-phase nanostructure. Increasing the substrate temperature and the nitrogen pressure in combination with a negative substrate bias provides the formation of a denser coating structure; the structure transforms from columnar to equiaxed.

The hardness of (TiHfZrVNb)N, formed by the process of separated vacuum arc deposition and reactive magnetron sputtering, increases from 23.4 GPa to 46.5 GPa when increasing the nitrogen concentration from 36% to 51.1% [34]. The structure of arc-deposited (AlCrTiZrNbY)N consists of two phases [38]: a nanocrystalline bcc phase (average crystallite size 15 nm, lattice period 0.342 nm) and a nanocrystalline fcc phase (average crystallite size 7 nm, lattice period 0.437 nm). Among the arc-deposited coatings, TiVZrNbHf nitride coatings formed at a nitrogen pressure of 0.27 Pa shows a very high hardness. Increasing the substrate bias from −50 V to −100 V at a coating texture orientation of [111] increases the coating hardness from 59 to 64 GPa, and at a biaxial orientation of [111] and [110] at −200 V, the hardness increases to 70 GPa; the crystallite size, which in this case measures 57 nm [40].

By now, many methods are available for HEA formation: powder metallurgy methods, hot pressing and casting technologies, etc. [41,42]. With promising prospects for the formation of metal coatings and hard (superhard) ceramic coatings based on HEAs, is the vacuum arc deposition method [43–52].

As a rule, the elemental composition, phase state, and defect substructure of metals and alloys are studied by scanning electron microscopy, transmission electron microscopy, and X-ray diffraction analysis. Recently, methods that use synchrotron radiation have been actively applied for research in the lattice state of growing HEA coatings.

The paper analyzes the structure and properties of metal, cermet, and ceramic NbMoCrTiAl coatings with the use of synchrotron radiation and other modern materials science methods.

The analysis extends the knowledge of HEA coatings formed by plasma-assisted vacuum arc deposition, including those with a metal–ceramic multilayer structure, which are poorly studied and little addressed in the literature.

2. Materials and Methods

The materials under study were metal, cermet, and ceramic NbMoCrTiAl coatings deposited on high-purity tungsten, 12Cr18Ni10Ti stainless steel, commercially pure titanium (Grade 2), and a hard WC–8%Co alloy. The gas-metal plasma for HEA coating deposition was produced on the QUINTA setup [53] with several different plasma generators operating at a time: a PINK-P gas plasma generator based on a non-self-sustained arc discharge with thermionic and hollow cathodes and four arc evaporators with niobium (99.8 wt.% Nb), titanium-aluminum (Ti–50 wt.% Al), molybdenum (99.96 wt.% Mo), and chromium (99.99 wt.% Cr) cathodes of diameter 80, 100, 100 mm and of dimensions 400 × 80 mm^2, respectively. All plasma generators, except for the evaporator with TiAl, were located on the chamber walls around a table with planetary satellites at equal distances from the chamber

center. The evaporator with TiAl was at the top of the chamber perpendicular to the other plasma generators. The experimental arrangement is described in detail elsewhere [54].

The contribution of the ion current of each arc evaporator was assessed by measuring the azimuthal characteristics of the ion current densities from the evaporators and PINK-P generator. The collector was located on a planetary satellite moving along the whole perimeter of the working chamber such that its spacing from all plasma generators was the same. The minimum distance from the generator exit aperture to the collector was 16 cm, and the maximum distance was 52 cm. The results of measurements are presented in Figure 1.
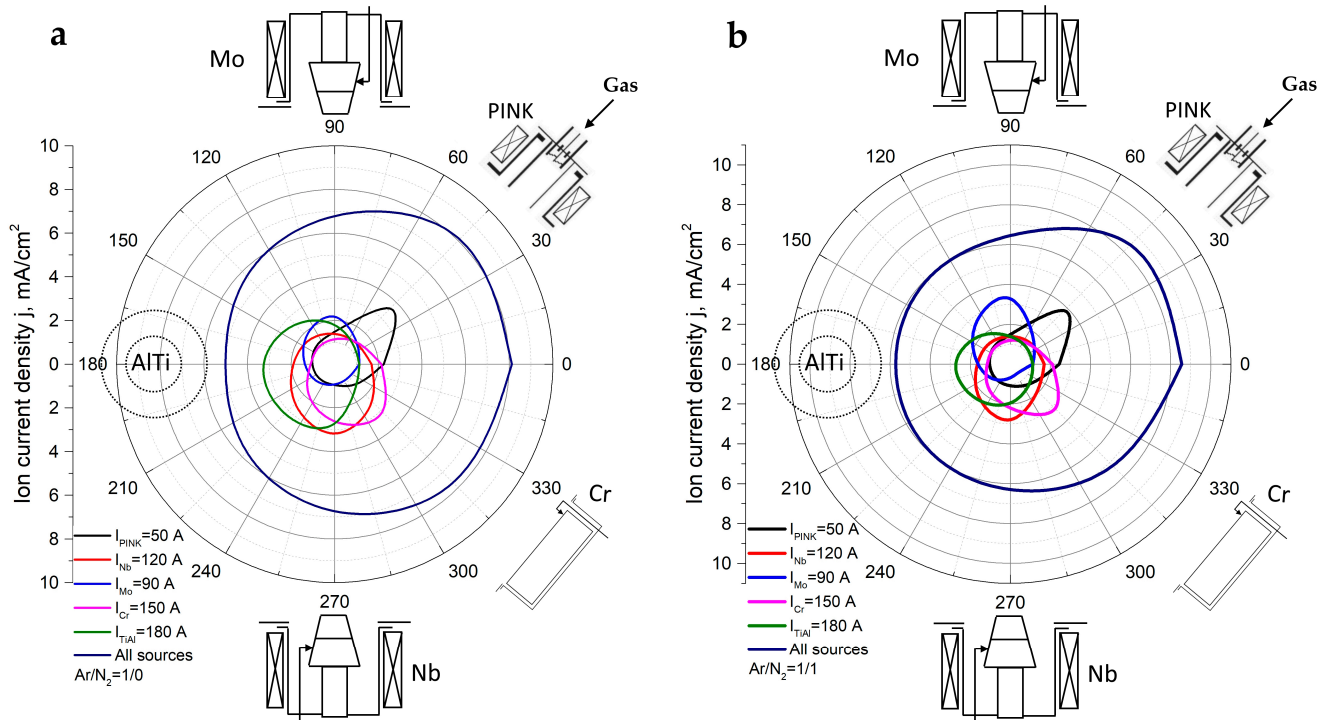

Figure 1. Azimuthal distribution of ion current density vs. arc current in argon (**a**) and mixture of argon and nitrogen in equal proportions (**b**).

The azimuthal ion current density distribution was used to determine the arc parameters at which the average ion current density to the collector was the same for all evaporators, measuring 2.45 mA/cm^2. Such conditions ensured the most uniform ion current density distribution over the chamber during simultaneous operation of the plasma generators, specified temperature level throughout the deposition of coatings, and coating thickness uniformity. The discharge currents of the metal plasma generators for the deposition of HEA coatings are tabulated in Table 1. The discharge current of the PINK-P gas plasma generator was 50 A. The substrates to be coated were fixed in a holder making an angle of 45° with the satellite rotation axis for uniform exposure to all types of plasma. The working gas was argon for the metal coating deposition and a mixture of argon and nitrogen in equal proportions for the ceramic coating deposition; the pressure in all experiments was 0.3 Pa. During the deposition, a negative pulsed bias was applied to the substrates. To optimize the mode of the HEA coating deposition, preliminary experiments were performed on the formation of coatings of different composition with separately and jointly operating plasma generators. The coatings formed in the experiments, in addition to HEA ones, were the following (Table 1): Nb, Mo, Cr, and TiAl, and NbN, MoN, CrN, and (Ti,Al)N, depending on the cathode material and gas mixture (argon and argon with nitrogen, respectively). The deposition time was 30 min. The coating thickness was measured by the Calotest method. The coating growth rates are given in Table 1. Reasoning from the preliminary experiments, metal and ceramic coatings 3 μm thick were formed.

Table 1. Discharge currents of metal plasma generators and coating growth rates.

Evaporated Cathode	Discharge Current, A	Coating Composition, Type	Coating Growth Rate, μm/h ± 10%.
Cr	150	Cr, metal CrN, ceramic	2.2 2.4
TiAl	180	TiAl, metal (Ti,Al)N, ceramic	2.4 5.2
Mo	90	Mo, metal MoN, ceramic	1.1 1.4
Nb	120	Nb, metal NbN, ceramic	0.9 2
Cr, TiAl, Mo, and Nb together	Discharge currents are indicated above	NbMoCrTiAl, metal (Nb,Mo,Cr,Ti,Al)N, ceramic NbMoCrTiAl/(Nb,Mo,Cr,Ti,Al)N, cermet	6.3 6 6.2

The deposition modes for multilayer cermet coatings were the same as those for metal and ceramic coatings, respectively. The deposition time of each metal and ceramic layer was chosen so that its thickness was 300 nm at a total number of layers of 10. Figure 2 shows a spherical section of such a coating of thickness 3 μm ± 10% after its Calotest. It is clearly seen that the cermet coating has a multilayer structure.
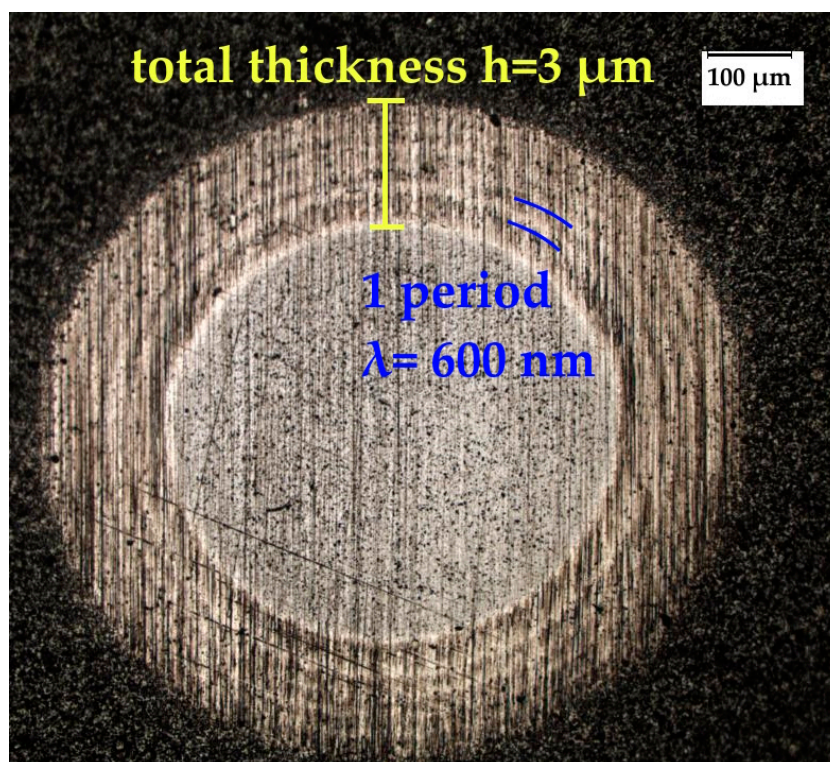
Figure 2. Characteristic spherical section of cermet coating on WC–8%Co alloy after the Calotest.

The elemental composition, phase state, and defect substructure of the coatings were examined on a Philips SEM-515 scanning electron microscope with an EDAX ECON IV microanalyzer and on a JEOL JEM-2100F transmission electron microscope. Their phase state and structure were analyzed on an XRD-6000 diffractometer in CuKα radiation (radiation wavelength λ = 1.540598 Å) in the standard Bragg–Brentano mode. The phase composition was analyzed using PDF 4+ databases and POWDER CELL 2.4 full-profile analysis

program. Additionally, these were investigated on the VEPP-3 storage ring in synchrotron radiation (INP SB RAS) under normal conditions (tungsten substrate, radiation wavelength $\lambda = 0.15401$ nm, diffraction angle $2\theta = 20°$–$80°$). The software was MAUD (structural analysis) and Fityk v.1.3.1 (data processing). The heat resistance of the coatings was measured by real-time X-ray diffractometry in synchrotron radiation on the VEPP-3 storage ring (Anton Paar HTK-2000 high-temperature X-ray chamber, OD-3M-350 one-dimensional position-sensitive detector, Fityk v.1.3.1 data processing software). The measurements were performed in air at an operating wavelength of 0.172 nm, temperature of 30–1300 °C, specimen heating rate of 15 °C/min, and exposure time of 1 min per frame. The diffraction angle 2θ was $28°$–$59°$. The hardness of the coatings was measured on a PMT-3 hardness tester (Vickers method, indenter load 0.5 N). Their physicomechanical properties were studied on a TTX-NHT nanohardness tester (acquisition rate 20.0 Hz, maximum linear load 30.0 mN, loading rate 60.00 mN/min, unloading rate 60.00 mN/min, pause 5.0 s, Poisson's ratio 0.25, Oliver–Pharr analysis), and their tribological properties were studied on a pin-on-disk tribometer and on an oscillating TRIBOtester (TRIBOtechnic, France) using a WC–8%Co ball of diameter 6 mm (load 2 N, wear track radius 2 mm, track length 50 m, ball velocity 25 mm/s). The wear of the coatings was determined from their wear track profilometry.

3. Results

Table 2 presents the elemental composition of the metal, cermet, and ceramic HEA coatings. It is readily seen that in terms of the relative content of metal atoms, the coatings fit the definition of high-entropy materials.

Table 2. Elemental composition of HEA coatings according to X-ray spectrum analysis.

HEA Coating Type	Elements, at %					
	Al	Ti	Cr	Nb	Mo	N
Metal	16.0	17.4	19.3	19.3	28.0	0.0
Cermet	9.7	17.2	11.2	17.7	21.1	23.1
Ceramic	13.9	6.8	9.3	6.8	7.8	55.4

As can be seen in Figure 3, the X-ray diffraction spectra of the three types of coating deposited on WC–8%Co and W have a much broader profile with respect to the reference lines of WC (Figure 3a) and W (Figure 3b). This suggests that the coatings can be both X-ray amorphous and nanocrystalline. The X-ray diffraction spectrum of the metal coating (Figure 3a, spectrum 1), unlike the others, reveals several peaks which allow one to determine the type and parameters of its lattice. Our analysis shows that the coating has a bcc lattice with $a = 0.3166$ nm. Note that Mo, Nb, and Cr contained in the HEA coating have this type of lattice.

The X-ray diffraction spectra measured via synchrotron radiation reveal broad peaks from HEA phases (Figure 3b). Judging from spectra 1, 3 in Figure 3b, the coatings have a structure close to that of Mo (bcc lattice); its unit cell parameter measures $a = 0.3146$ nm. The metal NbMoCrTiAl coating reveals peak asymmetry toward larger angles and likely because its metal peaks are superimposed. For the cermet coating (NbMoCrTiAl–(NbMoCrTiAl)N), even broader peaks of irregular shapes are observed, which can also be explained by the superposition of the peaks of its individual elements. The size of the coherent scattering regions is 5–6 nm for the metal coating and 2–3 nm for the cermet one. The X-ray diffraction spectrum of the ceramic coating has a single broad peak (Figure 3b, spectrum 2), which makes it impossible to determine the type and parameter of its lattice.

Our analysis by transmission and scanning transmission electron microscopy shows that the metal, ceramic, and cermet HEA coatings represent a multilayer film (Figure 4).
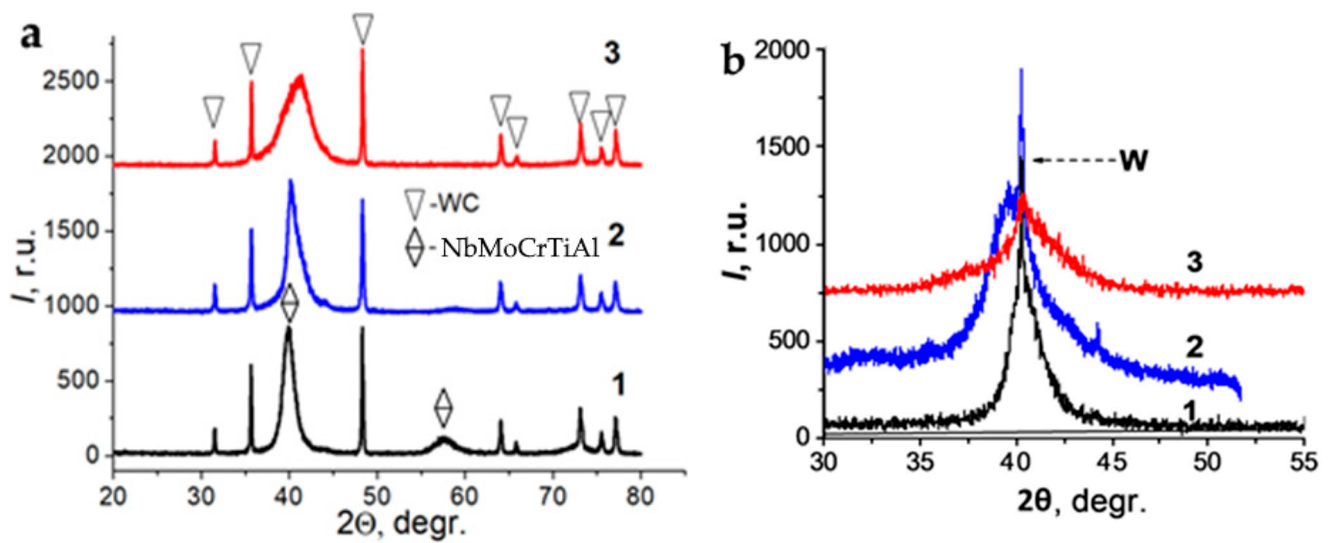
Figure 3. Fragments of X-ray diffraction spectra of metal (1), ceramic (2), and cermet HEA coatings (3) deposited on WC-8%Co (**a**) and W (**b**). Measurements on XRD-6000 diffractometer (**a**) and on VEPP-3 storage ring in synchrotron radiation (**b**).
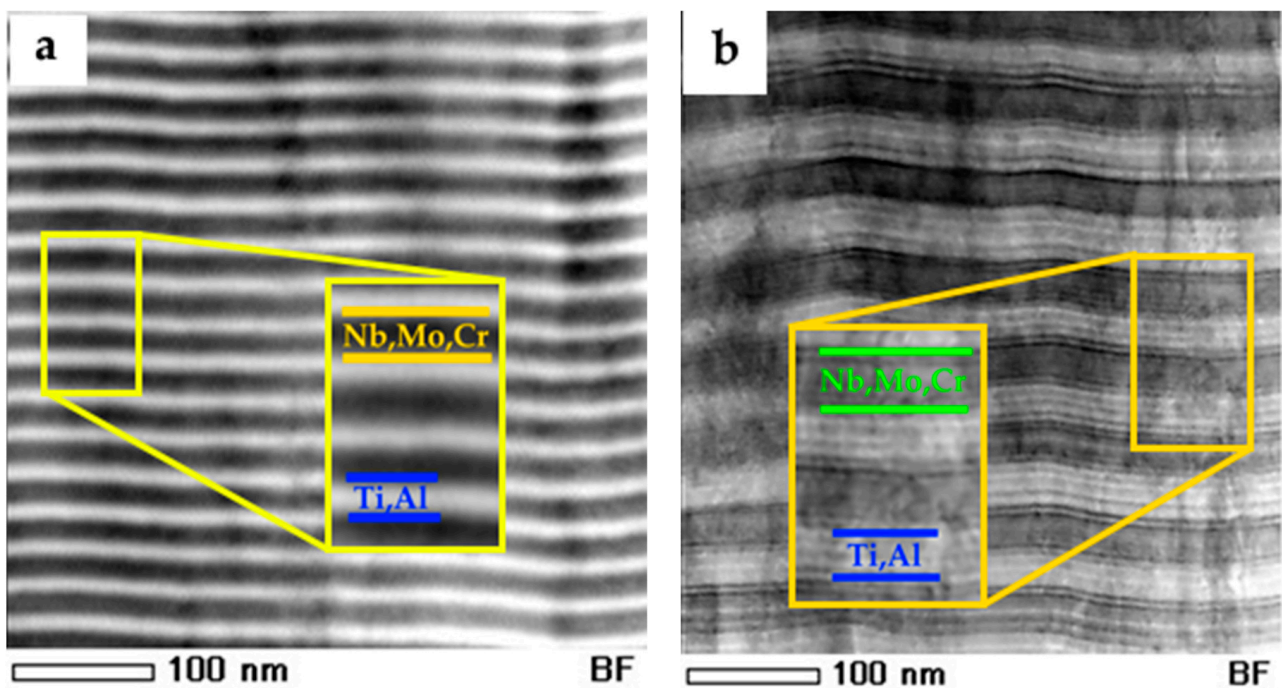

Figure 4. Structure of metal (**a**) and ceramic HEA coating (**b**). Scanning transmission electron microscopy.

According to the data from the X-ray spectrum analysis and X-ray mapping, the layers differ in elemental composition, which is exemplified for the metal and ceramic HEA coatings in Figures 5 and 6. As it follows from our analysis, the metal and ceramic coatings (Figure 4) are rich in Ti and Al in their bright layers and in Nb, Mo, and Cr in their dark layers; the nitrogen distribution over the ceramic coating volume is uniform.

It can be supposed that the main cause of the nonuniform element distribution is in the evaporation of four cathodes located on the chamber walls around the table with planetary satellites and from the location of the TiAl cathode at the top of the chamber perpendicular to the other cathodes.
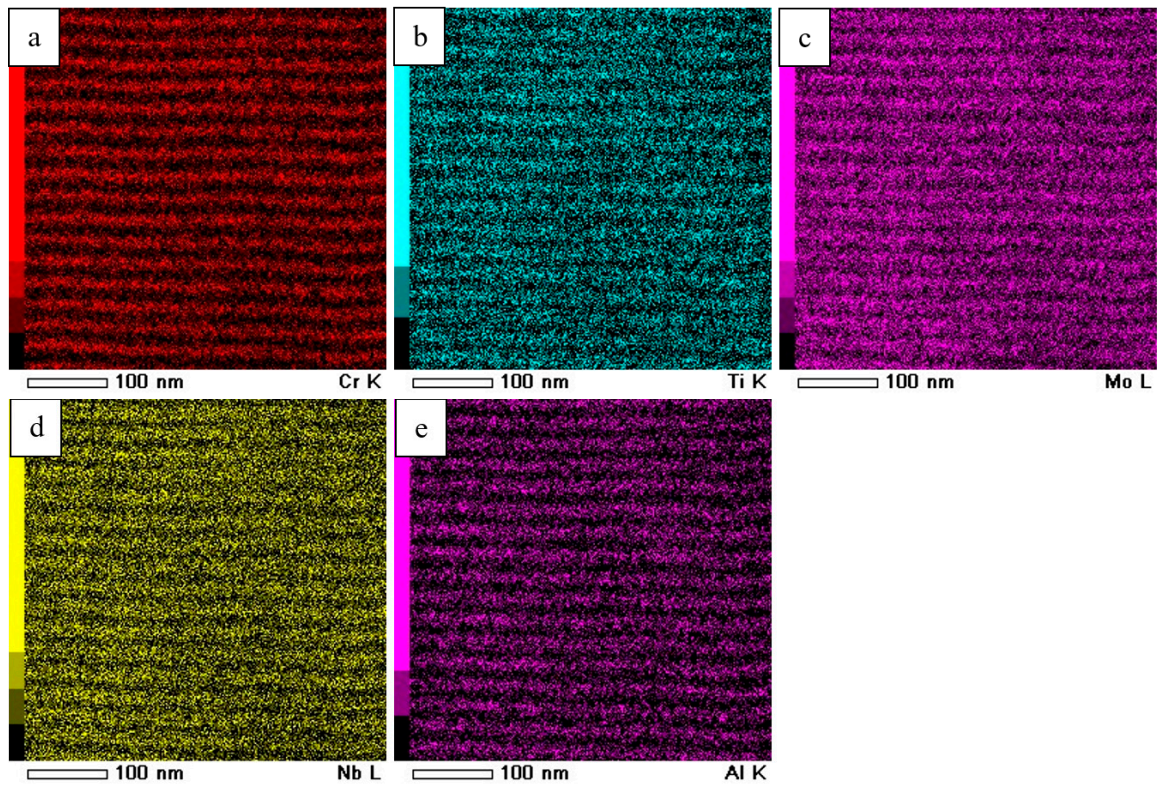
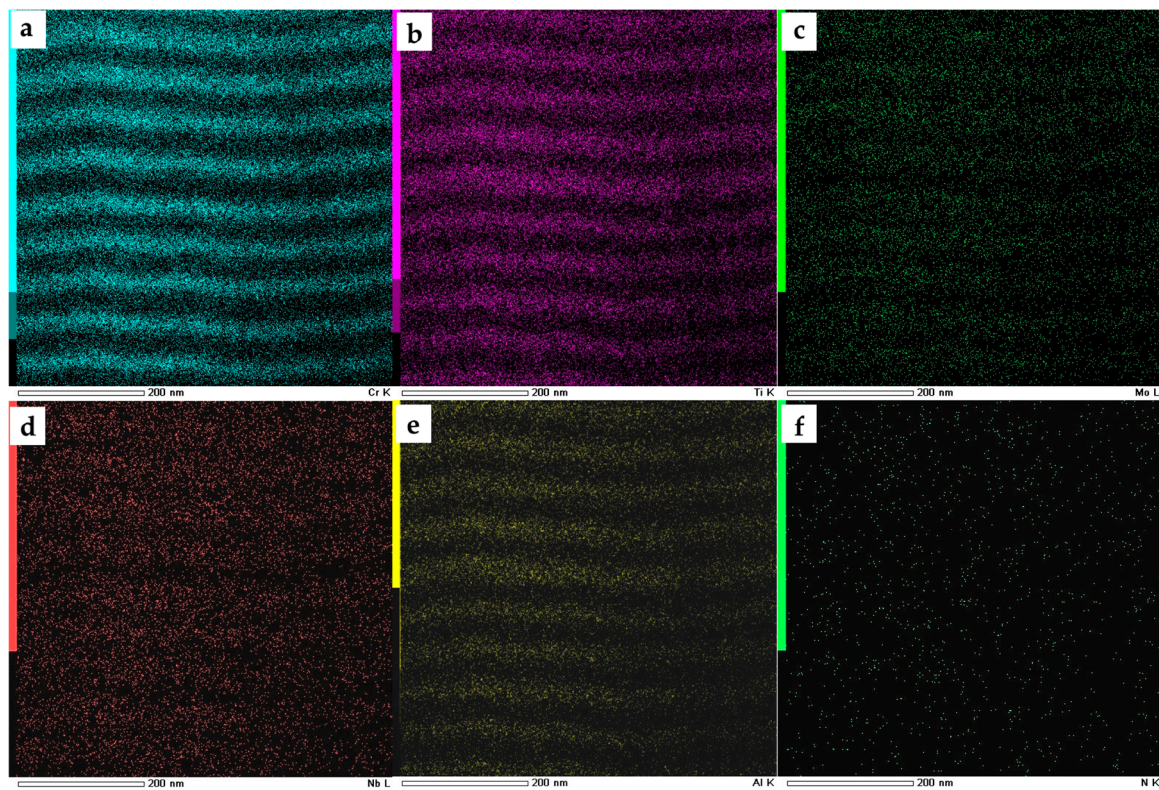**Figure 5.** Metal HEA coating in characteristic X rays from Cr (**a**), Ti (**b**), Mo (**c**), Nb (**d**), Al (**e**).

Figure 6. Ceramic HEA coating in characteristic X rays from Cr (**a**), Ti (**b**), Mo (**c**), Nb (**d**), Al (**e**), N (**f**).

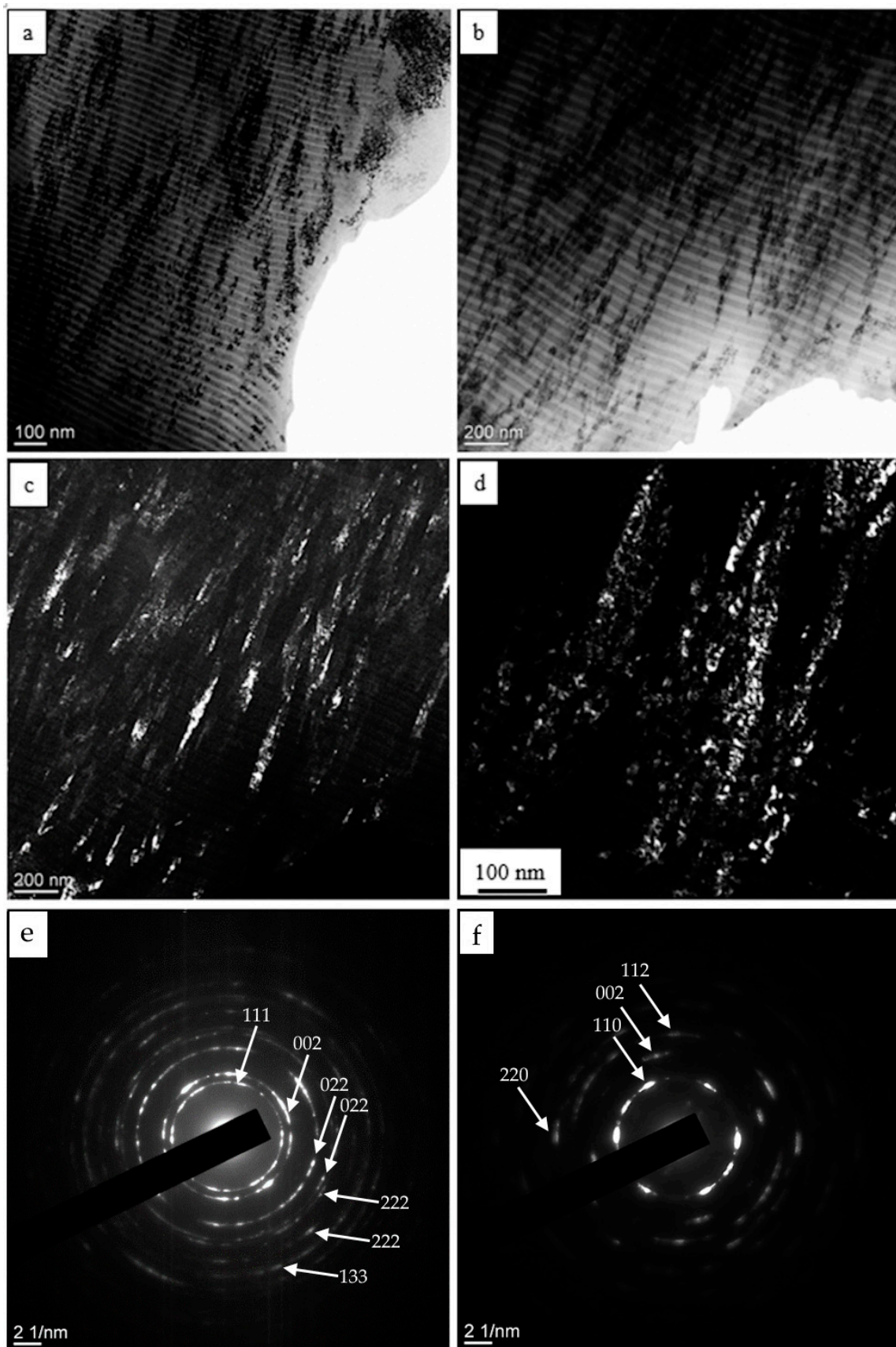Figure 7 shows the structure of the metal and ceramic coatings imaged by transmission electron microscopy.

Figure 7. Structure of metal (**a,d,f**) and ceramic HEA coatings (**b,c,e**) in bright field (**a,b**) and dark field (**c,d**), and electron diffraction patterns (**e,f**) with arrows for reflections in dark field.

The data in Figure 7 suggest that both coatings have a columnar structure (Figure 7c,d) formed by crystallites of size 3–5 nm (Figure 7d). The ratio of the diffraction ring radii (Figure 7e,f) attests that the metal and the ceramic HEA coating has a bcc and an fcc lattice, respectively.

The cermet HEA coating, as expected, consists of alternating nanocrystalline metal and ceramic layers with a bcc (Figure 8c,d) and an fcc lattice, respectively (Figure 8a,b).
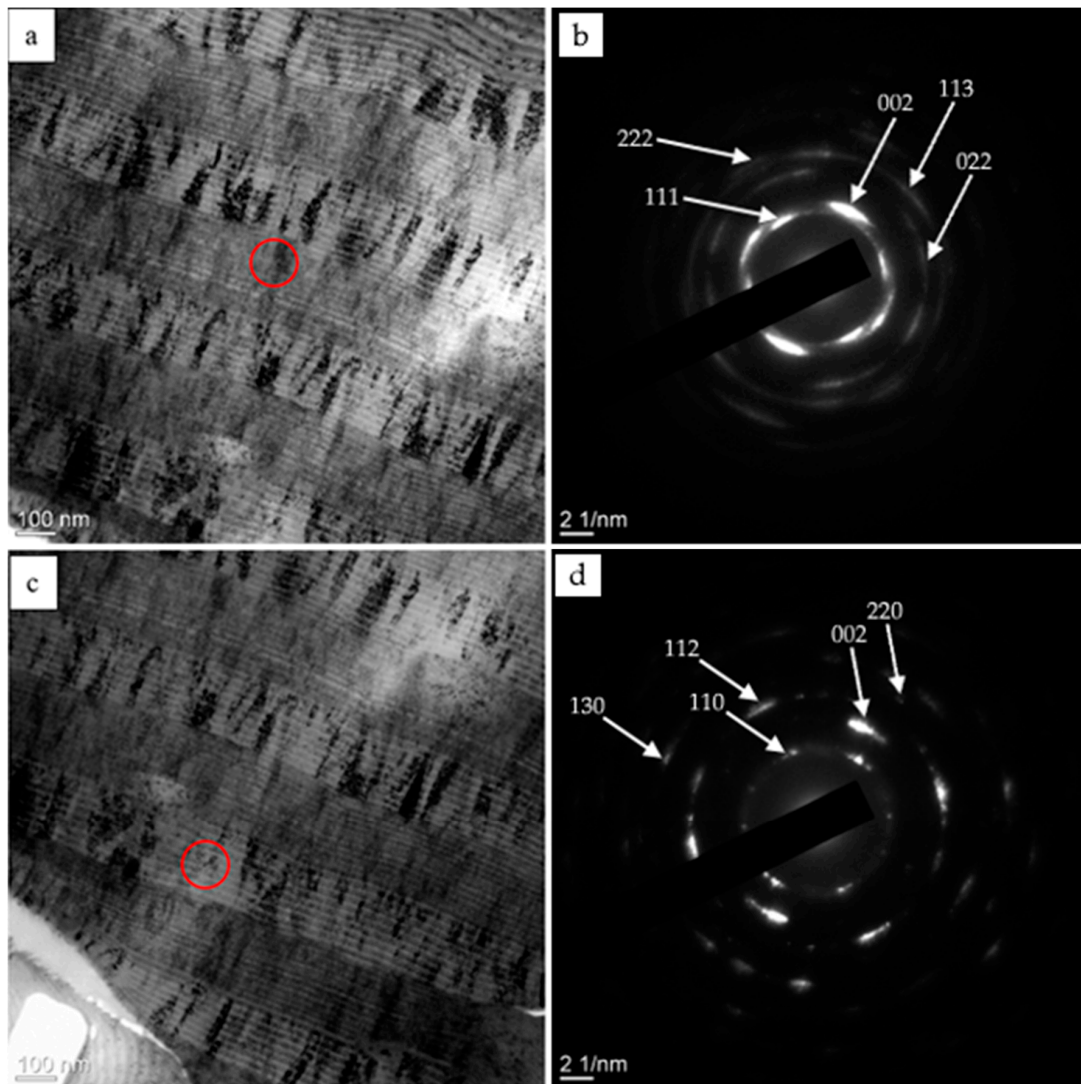

Figure 8. Structure of cermet HEA coating in bright field (**a,c**) and respective electron diffraction patterns (**b,d**) taken from its red-circled regions in (**a,c**).

It should be noted that the column height in the metal and ceramic coatings is much greater than the thickness of the individual layers (Figure 7) and can reach the total coating thickness, which adversely affects the crack resistance of the coatings. Such a columnar structure throughout the thickness of ceramic HAE coatings is described elsewhere [55]. In the cermet coating with alternating metal and ceramic layers, the column height is limited to the thickness of a single layer (Figure 8), which greatly increases its crack resistance compared to the metal and ceramic coatings. Besides, such cermet multilayer coatings have higher hardness, compared to metals, and higher fracture toughness, compared to single-phase ceramics [56].

The results of heat resistance tests with the use of synchrotron radiation (VEPP-3 storage ring) show that on heating in air, the ceramic coating starts to oxidize at 770–780 °C. The phase state of the heated coating is impossible to determine due to its thermal ex-

pansion and changes in the interplanar spacings of its reflections. At 1070–1080 °C, the X-ray patterns of the coating reveal new reflections presumably from oxides of the alloy elements. Further increasing the temperature shifts the reflections toward larger angles due to the deformation of the specimen and failure of the optical scheme. At ~1180 °C, all reflections previously present on the X-ray patterns disappear. On cooling to ~800 °C, intense reflections of the specimen holder are observed, suggesting that the stress arising in the coating deforms the specimen so that its surface comes out of the incident synchrotron radiation. Therefore, it is impossible to determine the final coating composition. Figure 9 presents the total set of X-ray patterns as projections of their intensity onto the diffraction angle–temperature plane for the ceramic HEA coating on a W substrate during heating in air from room temperature to 1300 °C.
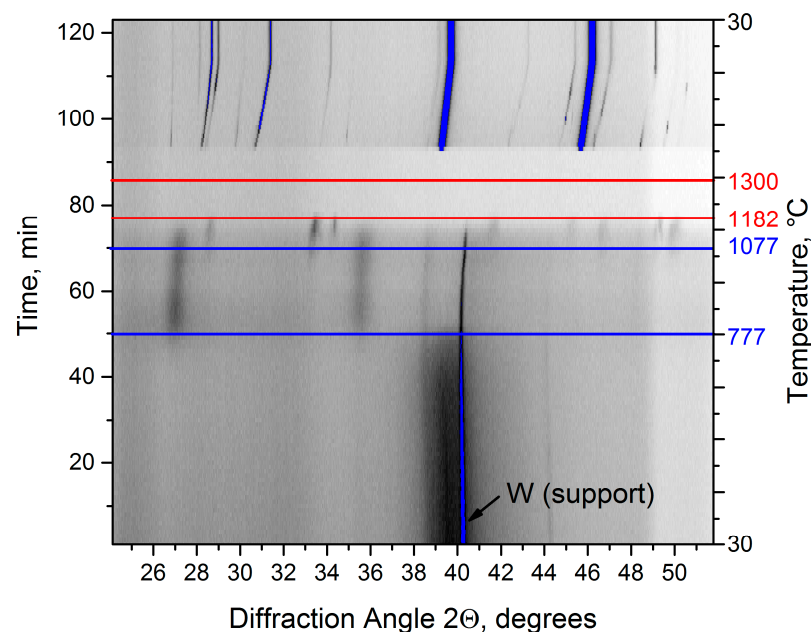

Figure 9. Total set of X-ray patterns as projections of their intensity onto a diffraction angle–temperature plane for ceramic HEA coating on a W substrate during heating in air from room temperature to 1300 °C.

The metal and cermet HEA coatings heated in air demonstrate almost the same behavior. At 630–640 °C, the coatings start to oxidize. At 1070–1080 °C, new reflections appear, presumably from oxides of their elements. At 1260–1270 °C, the HEA reflections disappear completely. Further, the coatings start to fail, and their final state is impossible to determine.

The mechanical and tribological parameters of the HEA coatings are presented in Table 3. The data presented allow the following conclusions. First, the metal HEA coating has a rather high hardness; the proportional summation of the hardness of its elements gives an HV = 1.1 GPa. Second, the hardness of the ceramic HEA coating is at the level of superhardness. In some cases [57,58], superhardness can be displayed by ceramic HEA coatings. Third, the wear resistance of the ceramic and cermet coatings is more than 20 times higher than that of the metal coatings. Such wear resistance is reported for the ceramic HEA and amorphous metal HEA coatings as well as for multilayer cermet coatings [58,59].

Table 3. Mechanical and tribological characteristics of HEA coatings.

Coating Type	HV, GPa	E, GPa	k, 10^{-5}, $mm^3N^{-1}m^{-1}$	μ
Metal	15	113	15	0.64
Cermet	27	176	0.64	0.20
Ceramic	43	326	0.65	0.47

4. Conclusions

In sum, we have analyzed the structure and properties of metal, cermet, and ceramic NbMoCrTiAl high-entropy alloy (HEA) coatings formed on solid substrates by the process of plasma-assisted vacuum arc deposition (from multicomponent gas-metal plasma through Nb, Mo, Cr, and TiAl cathode evaporation in argon and a mixture of argon and nitrogen). The analysis shows that all coatings represent a nanocrystalline (3–5 nm) film with a multilayer structure; the multilayer structure owes to the experimental technique used. The metal coating has a bcc lattice (a = 0.3146 nm). The ceramic coating has an fcc lattice; its parameter is uncertain due to highly smeared diffraction peaks. The hardness and Young's modulus of the coatings increase in the order of metal, cermet, and then ceramic, reaching 43 and 326 GPa, respectively. The wear resistance of the ceramic and cermet HEA coatings is more than 20 times higher than that of the metal one. On heating in air, the metal and cermet coatings start to oxidize at 630–640 °C, and the ceramic coating at 770–780 °C. At 1260–1270 °C, the coatings fail completely.

Conflicts of Interest: The authors declare no conflict of interest.

References

1. Cantor, B.; Chang, I.T.H.; Knight, P.; Vincent, A.J.B. Microstructural development in equiatomic multicomponent alloys. *Mater. Sci. Eng. A* **2004**, *375–377*, 213–218. [CrossRef]
2. Yeh, J.W.; Chen, S.K.; Lin, S.-J.; Gan, J.Y.; Chin, T.S.; Shun, T.-T.; Tsau, C.H.; Chang, S.Y. Nanostructured High-Entropy Alloys with Multiple Principal Elements: Novel Alloy Design Concepts and Outcomes. *Adv. Eng. Mater.* **2004**, *6*, 299–303. [CrossRef]
3. Chen, T.K.; Shun, T.T.; Yeh, J.W.; Wong, M.S. Nanostructured nitride films of multi-element high-entropy alloys by reactive DC sputtering. *Surf. Coat. Technol.* **2004**, *188–189*, 193–200. [CrossRef]
4. Chen, T.-K.; Wong, M.-S.; Shun, T.-T.; Yeh, J.-W. Nanostructured nitride films of multi-element high-entropy alloys by reactive DC sputtering. *Surf. Coat. Technol.* **2005**, *200*, 1361–1365. [CrossRef]
5. Kao, Y.-F.; Lee, T.-D.; Chen, S.-K.; Chang, Y.-S. Electrochemical passive properties of AlxCoCrFeNi (x = 0, 0.25, 0.50, 1.00) alloys in sulfuric acids. *Corros. Sci.* **2010**, *52*, 1026–1034. [CrossRef]
6. Ye, Q.; Feng, K.; Li, Z.; Lu, F.; Li, R.; Huang, J.; Wu, Y. Microstructure and corrosion properties of CrMnFeCoNi high entropy alloy coating. *Appl. Surf. Sci.* **2017**, *396*, 1420–1426. [CrossRef]
7. Senkov, O.N.; Wilks, G.B.; Scott, J.M.; Miracle, D.B. Mechanical properties of Nb25Mo25Ta25W25 and V20Nb20Mo20Ta20W20 refractory high entropy alloys. *Intermetallics* **2011**, *19*, 698–706. [CrossRef]
8. Wang, W.-R.; Wang, W.-L.; Wang, S.-C.; Tsai, Y.-C.; Lai, C.-H.; Yeh, J.-W. Effects of Al addition on the microstructure and mechanical property of AlxCoCrFeNi high-entropy alloys. *Intermetallics* **2012**, *26*, 44–51. [CrossRef]
9. Qiao, J.W.; Ma, S.G.; Huang, E.W.; Chuang, C.P.; Liaw, P.K.; Zhang, Y. Microstructural Characteristics and Mechanical Behaviors of AlCoCrFeNi High-Entropy Alloys at Ambient and Cryogenic Temperatures. *Mater. Sci. Forum* **2011**, *688*, 419–425. [CrossRef]
10. Laktionova, M.A.; Tabchnikova, E.D.; Tang, Z.; Liaw, P.K. Mechanical properties of the high-entropy alloy Ag0.5CoCrCuFeNi at temperatures of 4.2–300 K. *Low Temp. Phys.* **2013**, *39*, 630–632. [CrossRef]
11. Wu, J.-M.; Lin, S.-J.; Yeh, J.-W.; Chen, S.-K.; Huang, Y.-S.; Chen, H.-C. Adhesive wear behavior of AlxCoCrCuFeNi high-entropy alloys as a function of aluminum content. *Wear* **2006**, *261*, 513–519. [CrossRef]

12. Chuang, M.-H.; Tsai, M.-H.; Wang, W.-R.; Lin, S.-J.; Yeh, J.-W. Microstructure and wear behavior of AlxCo1.5CrFeNi1.5Tiy high-entropy alloys. *Acta Mater.* **2011**, *59*, 6308–6317. [CrossRef]
13. Zhou, Y.J.; Zhang, Y.; Wang, Y.L.; Chen, G.L. Solid solution alloys of AlCoCrFeNiTix with excellent room-temperature mechanical properties. *Appl. Phys. Lett.* **2007**, *90*, 181904. [CrossRef]
14. Zhang, Y.; Zuo, T.T.; Tang, Z.; Gao, M.C.; Dahmen, K.A.; Liaw, P.K.; Lu, Z.P. Microstructures and properties of high-entropy alloys. *Prog. Mater. Sci.* **2014**, *61*, 1–93. [CrossRef]
15. Lai, C.-H.; Lin, S.-J.; Yeh, J.-W.; Chang, S.-Y. Preparation and characterization of AlCrTaTiZr multi-element nitride coatings. *Surf. Coat. Technol.* **2006**, *201*, 3275–3280. [CrossRef]
16. Lin, C.; Duh, J.; Yeh, J.-W. Multi-component nitride coatings derived from Ti–Al–Cr–Si–V target in RF magnetron sputter. *Surf. Coat. Technol.* **2007**, *201*, 6304–6308. [CrossRef]
17. Chang, H.-W.; Huang, P.-K.; Davison, A.; Yeh, J.-W.; Tsau, C.-H.; Yang, C.-C. Nitride films deposited from an equimolar Al–Cr–Mo–Si–Ti alloy target by reactive direct current magnetron sputtering. *Thin Solid Film.* **2008**, *516*, 6402–6408. [CrossRef]
18. Tsai, M.-H.; Lai, C.-H.; Yeh, J.-W.; Gan, J.-Y. Effects of nitrogen flow ratio on the structure and properties of reactively sputtered (AlMoNbSiTaTiVZr)Nx coatings. *J. Phys. D Appl. Phys.* **2008**, *41*, 235402. [CrossRef]
19. Huang, P.-K.; Yeh, J.-W. Effects of nitrogen content on structure and mechanical properties of multi-element (AlCrNbSiTiV)N coating. *Surf. Coat. Technol.* **2009**, *203*, 1891–1896. [CrossRef]
20. Pogrebnjak, A.D.; Bagdasaryan, A.A.; Yakushchenko, I.V.; Beresnev, V.M. The structure and properties of high-entropy alloys and nitride coatings based on them. *Russ. Chem. Rev.* **2014**, *83*, 1027. [CrossRef]
21. Praveen, S.; Kim, H.-S. High-Entropy Alloys: Potential Candidates for High-Temperature Applications—An Overview. *Adv. Eng. Mater.* **2018**, *20*, 1700645. [CrossRef]
22. Pickering, E.J.; Jones, N.G. High-entropy alloys: A critical assessment of their founding principles and future prospects. *Int. Mater. Rev.* **2016**, *61*, 183–202. [CrossRef]
23. Nene, S.S.; Liu, K.; Frank, M.; Mishra, R.S.; Brennan, R.E.; Cho, K.C.; Li, Z.; Raabe, D. Enhanced strength and ductility in a friction stir processing engineered dual phase high entropy alloy. *Sci. Rep.* **2017**, *7*, 16167. [CrossRef]
24. Li, Z.; Körmann, F.; Grabowski, B.; Neugebauer, J.; Raabe, D. Ab initio assisted design of quinary dual-phase high-entropy alloys with transformation-induced plasticity. *Acta Mater.* **2017**, *136*, 262–270. [CrossRef]
25. Basu, S.; Li, Z.; Pradeep, K.G.; Raabe, D. Strain Rate Sensitivity of a TRIP-Assisted Dual-Phase High-Entropy Alloy. *Front. Mater.* **2018**, *5*, 30. [CrossRef]
26. Li, Z.; Tasan, C.C.; Springer, H.; Gault, B.; Raabe, D. Interstitial atoms enable joint twinning and transformation induced plasticity in strong and ductile high-entropy alloys. *Sci. Rep.* **2017**, *7*, 40704. [CrossRef] [PubMed]
27. Youssef, K.; Roberto, S.R. Applications of salt solutions before and after harvest affect the quality and incidence of postharvest gray mold of 'Italia' table grapes. *Postharvest Biol. Technol.* **2014**, *87*, 95–102. [CrossRef]
28. Miracle, D.B.; Miller, J.D.; Senkov, O.N.; Woodward, C.; Uchic, M.D.; Tiley, J. Exploration and Development of High Entropy Alloys for Structural Applications. *Entropy* **2014**, *16*, 494–525. [CrossRef]
29. Ashby, M.; Cebon, D.; Shercliff, H. *Materials: Engineering, Science, Processing and Design*; Butterworth-Heinemann: Oxford, UK, 2007.
30. Takeuchi, A.; Amiya, K.; Wada, T.; Yubuta, K.; Zhang, W.; Makino, A. Entropies in Alloy Design for High-Entropy and Bulk Glassy Alloys. *Entropy* **2013**, *15*, 3810–3821. [CrossRef]
31. Inoue, A.; Zhang, T.; Masumoto, T. Glass-forming ability of alloys. *J. Non-Cryst. Solids* **1993**, *156–158*, 473–480. [CrossRef]
32. Glicksman, M.E. *Principles of Solidification: An Introduction to Modern Casting and Crystal Growth Concepts*; Springer: New York, NY, USA, 2010.
33. Kumar, A.; Gupta, M. An Insight into Evolution of Light Weight High Entropy Alloys: A Review. *Metals* **2016**, *6*, 199. [CrossRef]
34. Komarov, F.F.; Pogrebnyak, A.D.; Konstantinov, S.V. Radiation Resistance of high-entropy nanostructured (Ti, Hf, Zr, V, Nb)N coatings. *Tech. Phys.* **2015**, *60*, 1519–1524. [CrossRef]
35. Tsai, D.-C.; Lin Huang, Y.; Lin, S.-R.; Liang, S.-C.; Shieu, F.-S. Effect of nitrogen flow ratios on the structure and mechanical properties of (TiVCrZrY)N coatings prepared by reactive magnetron sputtering. *Appl. Surf. Sci.* **2010**, *257*, 1361–1367. [CrossRef]
36. Liang, S.-C.; Chang, Z.-C.; Tsai, D.-C.; Lin, Y.-C.; Sung, H.-H.; Deng, M.-J.; Shieu, F.-S. Effects of substrate bias on structure and mechanical properties of (TiVCrZrHf)N coatings. *Appl. Surf. Sci.* **2011**, *257*, 7709–7713. [CrossRef]
37. Pogrebnjak, A.; Yakuschenko, I.; Bagdasaryan, A.; Bondar, O.; Krause-Rehberg, R.; Abadias, G.; Chartier, P.; Oyoshi, K.; Takeda, Y.; Beresnev, V.; et al. Microstructure, physical and chemical properties of nanostructured (Ti-Hf-Zr-V-Nb)N coatings under different deposition conditions. *Mater. Chem. Phys.* **2014**, *147*, 1079–1091. [CrossRef]
38. Beresnev, V.M.; Nemchenko, U.S.; Litovchenko, S.V.; Sobol, O.V.; Mejlekhov, A.A.; Postel'nik, A.A.; Gorban, G.F.; Stolbovoj, V.A.; Kolesnikov, D.A.; Novikov, V.Y. The influence of nitrogen pressure on the structure of condensates, obtained at vacuum-arc deposition from high entropy alloy AlCrTiZrNbY. *Vopr. At. Nauk. I Tekhniki* **2016**, *2-102*, 86–91.
39. Lai, C.-H.; Tsai, M.-H.; Lin, S.-J.; Yeh, J.-W. Influence of substrate temperature on structure and mechanical, properties of multi-element (AlCrTaTiZr)N coatings. *Surf. Coat. Technol.* **2007**, *201*, 6993–6998. [CrossRef]
40. Serdiuk, I.; Andreev, A.A.; Gorban', V.; Stolbovoi, V.; Sobol', O.; Krapivka, N.; Fil'chikov, V. Reproducibility of the Single-Phase Structural State of the Multielement High-Entropy Ti–V–Zr–Nb–Hf System and Related Superhard Nitrides Formed by the Vacuum-Arc Method. *Tech. Phys. Lett.* **2012**, *38*, 616–619. [CrossRef]

41. Gromov, V.E.; Ivanov, Y.F.; Osintsev, K.A.; Shlarova, Y.A.; Panchenko, I.A. High-entropy alloys: Structure and properties. Rusajns: Moscow, Russia, 2022; 204p.

42. Gromov, V.E.; Konovalov, S.V.; Ivanov, Y.F.; Osintsev, K.A. *Structure and Properties of High-Entropy Alloys*; Springer: Cham, Switzerland, 2021; 110p. [CrossRef]

43. Cherenda, N.N.; Rogovaya, I.S.; Shymanski, V.I.; Uglov, V.V.; Saladukhin, I.A.; Astashynski, V.M.; Kuzmitski, A.M.; Ivanov, Y.F.; Petrikova, E.A. Elemental and phase compositions and mechanical properties of titanium surface layer alloyed by zr, nb, and al under the action of compression plasma flows. *High Temp. Mater. Process. Int. Q. High-Technol. Plasma Process.* **2022**, *26*, 1–9. [CrossRef]

44. Tarbokov, V.A.; Slobodyan, M.; Pavlov, S.; Smolyanskiy, E.; Uglov, V.; Remnev, G.E. Changes in adhesion of crn coatings on zr-1%nb alloy substrates preliminary irradiated with high-intense pulsed ion beams. *High Temp. Mater. Process. Int. Q. High-Technol. Plasma Process.* **2022**, *26*, 7–19. [CrossRef]

45. Nikolaev, A.G.; Gushenets, V.I.; Bugaev, A.S.; Oks, E.M.; Vizir, A.V.; Yushkov, G.Y. Dc planar magnetron sputter deposition of boron thin films and their properties. *High Temp. Mater. Process. Int. Q. High-Technol. Plasma Process.* **2023**, *27*, 51–56. [CrossRef]

46. Ivanov, Y.F.; Shugurov, V.V.; Petrikova, E.A.; Krysina, O.V.; Prokopenko, N.A.; Tolkachev, O.S.; Petyukevich, M.S. Electron-ion-plasma synthesis of multilayer cr-b films. *High Temp. Mater. Process. Int. Q. High-Technol. Plasma Process.* **2023**, *27*, 11–18. [CrossRef]

47. Krysina, O.V.; Ivanov, Y.F.; Koval, N.N.; Prokopenko, N.A. The influence of plasma assistance modes on characteristics and composition of pvd zirconium nitride coatings. *High Temp. Mater. Process. Int. Q. High-Technol. Plasma Process.* **2023**, *27*, 19–31. [CrossRef]

48. Tyunkov, A.V.; Andronov, A.A.; Oks, E.M.; Yushkov, Y.G.; Zolotukhin, D.B. Analysis of formation and composition of boron-based protective coatings obtained by electron-beam deposition at fore-vacuum pressures. *High Temp. Mater. Process. Int. Q. High-Technol. Plasma Process.* **2023**, *27*, 65–73. [CrossRef]

49. Ivanov, Y.F.; Koval, N.N.; Krysina, O.V.; Baumbach, T.; Doyle, S.; Slobodsky, T.; Timchenko, N.A.; Galimov, R.M.; Shmakov, A.N. Superhard nanocrystalline Ti–Cu–N coatings deposited by vacuum arc evaporation of a sintered cathode. *Surf. Coat. Technol.* **2012**, *207*, 430–434. [CrossRef]

50. Krysina, O.V.; Koval, N.N.; Shmakov, A.N.; Vinokurov, Z.S. In situ X-ray diffraction investigation of nitride coatings at high-temperature oxidation. *J. Phys. Conf. Ser.* **2016**, *669*, 012034. [CrossRef]

51. Timchenko, N.A.; Zubavichus, Y.V.; Krysina, O.V.; Kuznetsov, S.I.; Syrtanov, M.S.; Bondarenko, S.V. Local structure of titanium nitride-based coatings. Journal of Surface Investigation. *X-Ray Synchrotron Neutron Tech.* **2016**, *10*, 425–428. [CrossRef]

52. Schroeder, J.L.; Thomson, W.; Howard, B.; Schell, N.; Näslund, L.-Å.; Rogström, L.; Johansson-Jõesaar, M.P.; Ghafoor, N.; Odén, M.; Nothnagel, E.; et al. Industry-relevant magnetron sputtering and cathodic arc ultra-high vacuum deposition system for in situ x-ray diffraction studies of thin film growth using high energy synchrotron radiation. *Rev. Sci. Instrum.* **2015**, *86*, 095113. [CrossRef]

53. Shugurov, V.V.; Koval, N.N.; Krysina, O.V.; Prokopenko, N.A. QUINTA equipment for ion-plasma modification of materials and products surface and vacuum arc plasma-assisted deposition of coatings. *J. Phys. Conf. Ser.* **2019**, *1393*, 012131. [CrossRef]

54. Ivanov, Y.F.; Koval, N.N.; Akhmadeev, Y.H.; Uglov, V.V.; Shugurov, V.V.; Petrikova, E.A.; Krysina, O.V.; Prokopenko, N.A.; Azhazha, I.I. Structure and Properties of Multi-Layer Films of High-Entropy Metals Deposited by the Ion-Plasma Method. *Russ. Phys. J.* **2022**, *64*, 2207–2213. [CrossRef]

55. Chang, Y.-Y.; Chung, C.-H. Tribological and Mechanical Properties of Multicomponent CrVTiNbZr(N) Coatings. *Coatings* **2021**, *11*, 41. [CrossRef]

56. Wang, Y.; Li, M.; Wang, H.; Shao, G.; Zhu, J.; Liu, W.; Wang, H.; Fan, B.; Xu, H.; Lu, H.; et al. The Fabrication and Mechanical Properties of Laminated ZrB_2-Mo_5SiB_2 Ceramics with an Mo-Mo_5SiB_2 Interlayer. *Metals* **2021**, *11*, 2018. [CrossRef]

57. Padamata, S.K.; Yasinskiy, A.; Yanov, V.; Saevarsdottir, G. Magnetron Sputtering High-Entropy Alloy Coatings: A Mini-Review. *Metals* **2022**, *12*, 319. [CrossRef]

58. Devarajan, D.K.; Rangasamy, B.; Amirtharaj Mosas, K.K. State-of-the-Art Developments in Advanced Hard Ceramic Coatings Using PVD Techniques for High-Temperature Tribological Applications. *Ceramics* **2023**, *6*, 301–329. [CrossRef]

59. Grigoriev, S.N.; Sobol, O.V.; Beresnev, V.M.; Serdyuk, I.V.; Pogrebnyak, A.D.; Kolesnikov, D.A.; Nemchenko, U.S. Tribological characteristics of (TiZrHfVNbTa)N coatings applied using the vacuum arc deposition method. *J. Frict. Wear* **2014**, *35*, 359–364. [CrossRef]